Modelling Li-ion cell thermal runaway triggered by an internal short circuit device using an efficiency factor and Arrhenius formulations

Coman, Paul Tiberiu ; Darcy, Eric; Veje, Christian ; White, Ralph

Published in:
Journal of The Electrochemical Society

DOI:
10.1149/2.0341704jes

Publication date:
2017

Document version:
Final published version

Modelling Li-Ion Cell Thermal Runaway Triggered by an Internal Short Circuit Device Using an Efficiency Factor and Arrhenius Formulations

Paul T. Coman,[a,z] Eric C. Darcy,[b] Christian T. Veje,[c] and Ralph E. White[d,*]

[a]*Mads Clausen Institute, University of Southern Denmark, 6400 Sønderborg, Denmark*
[b]*NASA Johnson Space Center, Houston, Texas 77058, USA*
[c]*Center for Energy Informatics, University of Southern Denmark, 5230 Odense, Denmark*
[d]*Department of Chemical Engineering, University of South Carolina, Columbia, South Carolina 29208, USA*

This paper presents a novel model for analyzing thermal runaway in Li-ion battery cells with an internal short circuit device implanted in the cell. The model is constructed using Arrhenius formulations for representing the self-heating chemical reactions and the State of Charge. The model accounts for a local short-circuit, which is triggered by the device embedded in the cell windings (jelly roll). The short circuit is modeled by calculating the total available electrical energy and adding an efficiency factor for the conversion of electric energy into thermal energy. The efficiency factor also accounts for the energy vented from the cell. The results show good agreement with the experimental data for two cases – a 0D model and a 3D model of a single cell. Introducing the efficiency factor and simplifying the short-circuit modeling by using an Arrhenius formulation reduces the calculation time and the computational complexity, while providing relevant results about the temperature dynamics. It was found that for an 18650 NCA/graphite cell with a 2.4 Ah capacity, 28% of the electrical energy leaves with the effluent.

Manuscript submitted October 18, 2016; revised manuscript received November 30, 2016. Published January 28, 2017.

Lithium-ion batteries are gaining more and more popularity in the field of electric energy storage.[1] This trend is followed by an increase in safety, energy density, and cycle life requirements. The increase in energy density brought a significant contribution to this trend, but it came with a trade-off concerning safety.[2,3] When operated under abusive conditions such as overcharging, over-discharging, object penetrations or even operation under high ambient temperatures, etc., Li-ion batteries can undergo internal short circuits between the current collectors or electrodes, leading to thermal runaway.[3] The reactions with electrolyte inside the cell decompose the battery components, generating a significant amount of heat, which, if not properly managed can lead to fires and explosions.[4] To assist the design of thermal management systems in mitigating the effects of thermal runaway, it is important to be able to model thermal runaway and account for the energy contributions in the process.

Modeling thermal runaway has been the focus of many researchers, but the authors in Refs. 5,6 brought a substantial contribution to the field. The authors found the activation energies and the enthalpies of the different decomposition reactions for the components in an 18650 LCO (2.6 Ah) Li-ion battery and proposed a model for predicting thermal runaway based on Arrhenius formulations. Papers such as Refs. 7,8 added new decomposition reactions (cathode, electrolyte) and extended the model, from a simplified lumped model to complex 2D and 3D geometries for a single cell. Based on these models, some authors extended the models to simulate the thermal behavior of single battery cells.[9] A comprehensive list of references and studies of modeling safety in Li-ion is given in Ref. 3. The activation energies and the enthalpies found by the authors in Refs. 5, 6 are crucial for predicting the energy released during thermal runaway and are used in this paper.

During a thermal runaway, an internal short circuit (ISC) can occur in the cell due to a conducting metal particle, component defects or melting of the separator, causing the adjacent electrodes (the anode and the cathode) to come into contact. Analyzing the ISC is a challenging task being tackled by more and more authors. Some focused on experimental studies on different types of cells,[10–13] but only a few studies have been performed in modeling the ISC.[14–17] In Ref. 17 the authors modeled the short-circuit by coupling a P2D (pseudo two-dimensional) porous electrode model with a thermal model, while the authors in Ref. 18 used an equivalent circuit model. Both methods are well defined and give good results, but they are complex, and the P2D method requires parameters that are not easy to determine.

Recently, a patent for an internal short circuit device (ISCD) was published in Ref. 19, opening a new way for testing battery safety. The ISCD is a wax-based device implanted in the cell, which triggers a short circuit with a small amount of energy input, due to the low melting temperature of the wax (57°C). The ISCD thus accelerates the occurrence of the thermal runaway process in comparison to oven heating, for example.

The device was investigated experimentally by the authors in Refs. 20–22, while its effectiveness and functionality were demonstrated in battery packs for space applications in Ref. 23. The authors showed that an ISCD is very practical for investigating thermal runaway propagation in packs. By using an X-ray tomography, the authors in Ref. 24 investigated the thermal runaway behavior of a cell with an ISCD, showing the structural dynamics and the position of the ISCD. The authors also showed that the thermal runaway event triggered with such a device resulted in a sudden temperature rise around the temperature reading corresponding to the melting point of the wax, which indicates that the venting event occurs simultaneously with the decomposition reactions in a very short time.

In Ref. 25 the authors present general information about the ISCD and their institute's capability to model thermal runaway triggered by the device. However, no detailed modeling has been published in the open literature for investigating the thermal runaway in 18650 cells with the ISCD.

The aim of this paper is to formulate a simple model for modeling thermal runaway in 18650 NCA/graphite cells with an ISCD. The model requires only a few parameters for simulating thermal runaway triggered by such a device. The model is built by using an Arrhenius formulation and an efficiency factor. A similar approach was used in a previous paper,[26] where the State of Charge (SoC) was modeled as a simplified chemical reaction. However, in this study, the triggering time can be estimated by knowing the melting temperature of the wax inside the ISCD, and therefore the electrochemical reaction can be simplified even further.

An Arrhenius formulation for the SoC is used here because of its simplicity, assuming that during the short circuit, the electrical energy

*Electrochemical Society Fellow.
[z]E-mail: paulcoman@mci.sdu.dk

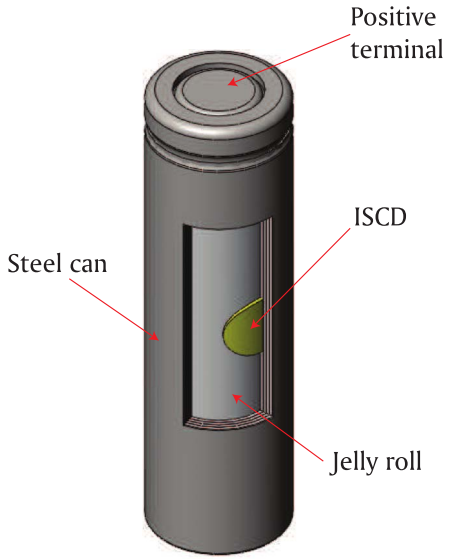

Figure 1. Sketch of an 18650 battery cell used for visualizing the ISCD and its position relative to the steel can.

is converted into thermal energy following a chemical reaction.[26] Finally, an efficiency factor is included in the model (conversion of electrical energy to thermal energy and venting), and a 0D study and a 3D study are performed for investigating the validity of this assumption.

The model is validated against the experimental data provided by the Battery Team from NASA JSC (Johnson Space Center). A battery cell with an ISCD is used to trigger a single cell into thermal runaway on-demand to verify the safety features of space battery designs.[21]

Experimental

For the experimental procedure, a cylindrical 18650 NCA/graphite Moli cell with a capacity of 2.4 Ah and a wax-based ISCD implanted in the separator was used[24] (Figure 1).

The wax melts at around 57°C, causing the electrodes to short-circuit (anode active to collector short-circuit type[20]). This particular cell was chosen for experimentation in order to demonstrate the usability of the device and to ensure that the trigger cell is driven into a thermal runaway with minimal heat input. The experimental set-up can be seen in Figure 2.

Two thermocouples were welded on the surface of the cell; one at the bottom and one on the side (at the middle of the cell height). The cell was fixed with wires on a vertical support and lifted off the ground for accommodating the bottom thermocouple. Two patch heaters were attached on both sides of the cell, close to the bottom and diametrically opposed, as indicated with red in Figure 2.

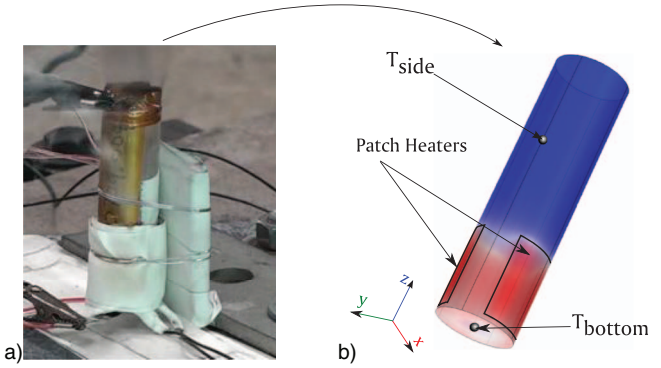

Figure 2. Snapshot of a single battery cell used in the experiment (a) and the sketch indicating the position of the thermocouples (b). For this experiment, two electric patch heaters were used for heating up the cell.

The heaters were wrapped with insulating weave to reduce the heat losses to the ambient. For the experiment, the cell was fully charged to 4.2 V. The power of the heater, the voltage of the cell and the temperature readings from the two thermocouples were recorded at a resolution of 0.1 seconds for the duration of the experiment. The heater power and the voltage of the cell are shown in Figure 3.

The heaters were connected to a power supply and set to deliver 60 W. However, due to the high power, the cables and the connections overheated and some parts of the insulation were burned, losing power. For this reason, the power of the heater was continuously increased to overcome the losses, as seen in Figure 3. After reaching a maximum value of 80 W, the power dropped due to losses and then increased again. Once the melting point of the wax was reached, the cell went into thermal runaway. At this point, the voltage reading dropped to zero due to ISC, and few seconds after, the heater was turned off to avoid the extra heat input. The temperatures measured experimentally are used to validate the model, as seen in results section.

Mathematical Model

The electrochemical model.—The mathematical model is formulated using the Arrhenius equations for the different reactions – *the decomposition of the anode*, *cathode* and *SEI (Solid Electrolyte Interface)* – and for the *SoC*. The equations for a single cell jelly roll domain are given below:[5]

$$\frac{dx_a}{dt} = -x_a \cdot A_a \cdot exp\left(-\frac{E_a}{k_b T}\right) \cdot exp\left(-\frac{z}{z_0}\right) \quad [1]$$

$$\frac{dz}{dt} = x_a \cdot A_a \cdot exp\left(-\frac{E_a}{k_b T}\right) \cdot exp\left(-\frac{z}{z_0}\right) \quad [2]$$

$$\frac{dx_s}{dt} = -x_s \cdot A_s \cdot exp\left(-\frac{E_s}{k_b T}\right) \quad [3]$$

$$\frac{d\alpha}{dt} = \alpha(1-\alpha) \cdot A_c \cdot exp\left(-\frac{E_c}{k_b T}\right) \quad [4]$$

$$\frac{dSoC}{dt} = -ISC_{cond} \cdot SoC \cdot A_{ec} \cdot exp\left(-\frac{E_{ec}}{k_b T}\right) \quad [5]$$

Equations 1–4 are the generic equations that describe the decomposition reactions based on the fraction of Li present in the anode and SEI (x_a and x_s), but also on the degree of conversion of the cathode (α). In addition to this, the change in the SEI thickness (z) is added to the decomposition of the anode (tunneling effect[6,27]). Equation 5 is developed for calculating the state of charge, which changes during thermal runaway. This equation is a simplification of the SoC equation used previously in Ref. 26, and it is adopted because of the short-circuit trigger time instance, which is approximated by knowing the melting temperature of the wax. For a more comprehensive formulation, there are many papers where the authors developed correlations for estimating or controlling the SoC.[28–32] The activation energy for Equation 5 (E_{ec}) is fitted to match the activation energy of a simple reaction that has a self-heating behavior around the melting point of the ISCD (T_{ISC} = 57°C). An extra factor (ISC_{cond}) is used in Equation 5 to make sure that the reaction is activated only after the ISC trigger temperature. The factor ISC_{cond} is defined as follows:

$$ISC_{cond} = \begin{cases} 0 \, for \, T < 57\,^{\circ}C \\ 1 \, for \, T \geq 57\,^{\circ}C \end{cases} \quad [6]$$

The temperature (T) in Equations 1–6 is averaged over the volume to achieve fast calculations, as explained later in the 0D Model (Lumped model) section.

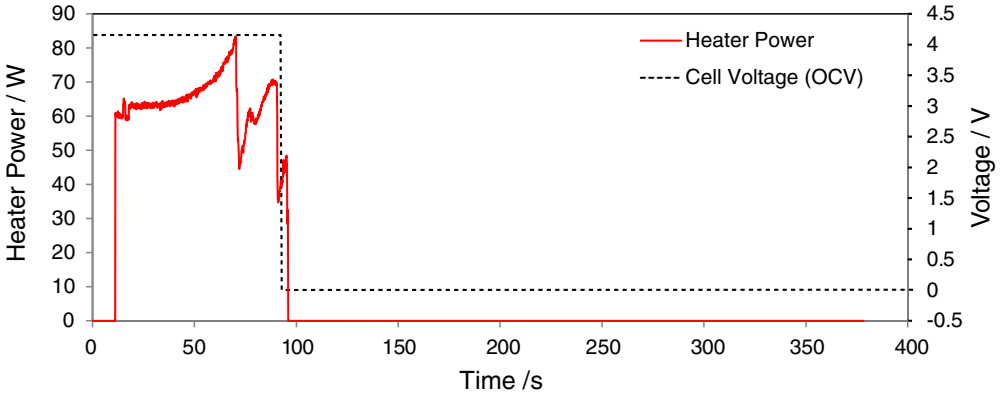

Figure 3. Plot showing the power of the heaters and the open cell voltage of the 18650 Moli NCA/graphite measured experimentally.

Thermal model.—The thermal model is given by a generic thermal diffusion equation with an internal heat source:

$$\rho C_p \frac{dT}{dt} = \nabla \cdot (k \nabla T) + \frac{\dot{Q}_{exo}}{V_{cell}} \quad [7]$$

In Eq. 7, the terms ρ, C_p, k and T correspond to each domain (jelly roll and steel casing) in the 3D study. For the 0D case, an average value of temperature and effective values are used for ρ and C_p, as described in more detail in The 0D Model (Lumped model) section. The cell dissipates heat through convection and radiation to the ambient, and the patch heaters are modeled as a surface heat flux (the surface covered by the heat flux is $A_{patch} = 2 \cdot H_{patch} \cdot L_{patch}$). The heat source term ($\dot{Q}_{exo}$) in Eq. 7 corresponds to the exothermic reactions and is valid only for the jelly roll domain where the decomposition reactions occur. The heat coming from the patch heaters is modeled as a heat flux which vanishes when the jelly roll temperature reaches 170°C (the heater is turned off when the cell goes into thermal runaway). Considering that the power loss in the wires and connections are high, the power of the heaters is fitted to match the heating rate of the cell, and a constant value is used instead of a heating profile. The value of the heater power is given in Table I.

The heat source term ($\dot{Q}_{exo}$) is defined as follows:

$$\dot{Q}_{exo} = \dot{Q}_a + \dot{Q}_c + \dot{Q}_s + \dot{Q}_{ec} \quad [8]$$

where each term is given as:

$$\dot{Q}_a = -m_a h_a \frac{dx_a}{dt} \quad [9]$$

$$\dot{Q}_c = m_c h_c \frac{d\alpha}{dt} \quad [10]$$

$$\dot{Q}_s = -m_a h_s \frac{dx_s}{dt} \quad [11]$$

$$\dot{Q}_{ec} = -h_{ec} \frac{dSoC}{dt} \quad [12]$$

The minus signs are chosen to make sure that the effects are exothermic. The enthalpies in Eqs. 9–11 do not need any corrections. On the other hand, the enthalpy term in Eq. 12 (h_{ec}) is given as:

$$h_{ec} = V \cdot C \cdot 3600 \cdot \eta \quad [13]$$

The electrical-thermal conversion term (η) represents the efficiency factor which accounts for how much electrical energy is converted into heat, and for the energy leaving with venting. From a previous study,[26] it was found that venting of electrolyte and ejecta contribute to the energy tally, thus for this study, the effects of venting of energy are not directly considered, but included in an efficiency factor (η), which takes values from 0 to 1, and is fitted to match the experiments.

A visual interpretation of the energy tallying can be seen in Figure 4.

This approach reduces the number of parameters that are required to be fitted, in order to match the experimental data, i.e. from at least four parameters (used for modeling the electrolyte venting, ejecta venting, vaporization, pressure increase, etc.) to only one – the efficiency factor, which includes the effect of venting. The efficiency (η) is described in more detail in Results 0D Model section.

Modeling Procedures

The 3D model.—The 3D geometry study is performed using the Finite Element tool – COMSOL Multiphysics v.5.1. The geometry is discretized in a mesh network, and the temperature field (T) is calculated in each node of the network. However, for achieving fast calculations, the temperature in the thermal model is evaluated in

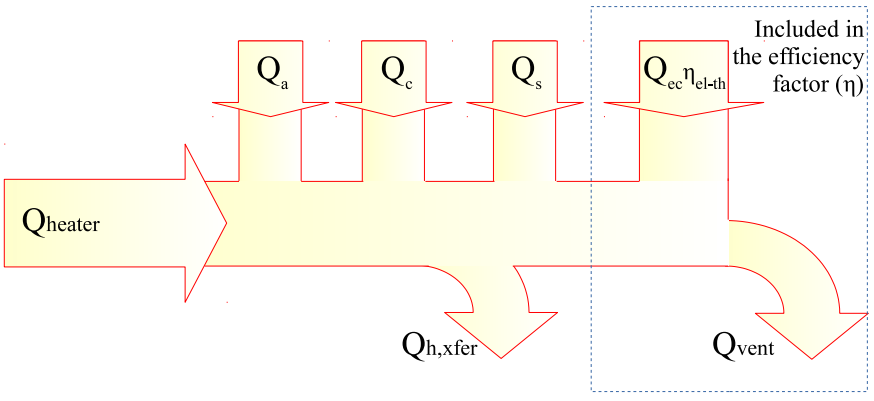

Figure 4. Energy tally sketch, including the exothermic reactions and the energy leaving by venting. The energy due to venting of electrolyte and ejecta is subtracted from the total electrochemical energy by introducing the efficiency factor (η).

Table I. The parameters used for solving Equations 1–15.

Parameter	Value	Unit	Source
A_a	$2.5 \cdot 10^{13}$	s^{-1}	Ref. 5
A_c	$6.67 \cdot 10^{11}$	s^{-1}	Ref. 5
A_{ec}	$3.37 \cdot 10^{12}$	s^{-1}	Fit.
A_s	$1.67 \cdot 10^{15}$	s^{-1}	Ref. 5
A_{patch}	$7.25 \cdot 10^{-4}$	m^2	Meas.
A_{surf}	$3.5 \cdot 10^{-3}$	m^2	Meas.
C	2.4	Ah	Meas.
Cp_{can}	460	$J\ kg^{-1}\ K^{-1}$	Ref. 5
Cp_{jr}	830	$J\ kg^{-1}\ K^{-1}$	Ref. 5
E_a	$2.24 \cdot 10^{-19}$	J	Ref. 5
E_c	$2.03 \cdot 10^{-19}$	J	Ref. 5
E_{ec}	$1.58 \cdot 10^{-19}$	J	Fit.
E_s	$2.24 \cdot 10^{-19}$	J	Ref. 5
h_a	1714	$J\ g^{-1}$	Ref. 5
H_{batt}	$65 \cdot 10^{-3}$	m	Meas.
h_c	314	$J\ g^{-1}$	Ref. 5
h_{conv}	7	$W\ m^{-2}\ K^{-1}$	Ref. 5
h_{ec}	10.17	kJ	Calc.
h_{res}	50	$W\ m^{-2}\ K^{-1}$	Ref. 33
H_{patch}	$19.1 \cdot 10^{-3}$	m	Meas.
h_s	257	$J\ g^{-1}$	Ref. 5
k_{can}	14	$W\ m^{-1}\ K^{-1}$	Ref. 5
k_{jr}*	(3.4, 3.4, 28)*	$W\ m^{-1}\ K^{-1}$	Ref. 37
L_{patch}	$9.15 \cdot 10^{-3}$	m	Meas.
m_a	$8.1 \cdot 10^{-3}$	kg	Ref. 38
m_c	$18.3 \cdot 10^{-3}$	kg	Ref. 38
r_{cell}	$9 \cdot 10^{-3}$	m	Meas.
r_{jr}	$8.9 \cdot 10^{-3}$	m	Meas.
SoC_0	1	-	Approx.
T_{amb}	20	°C	Meas.
t_{can}	$0.125 \cdot 10^{-3}$	m	Meas.
T_{init}	20	°C	Meas.
T_{ISC}	57	°C	Ref. 39
V	4.2	V	Meas.
V_{cell}	$1.663 \cdot 10^{-5}$	m^3	Meas.
$x_{a,0}$	0.75	-	Ref. 5
$x_{s,0}$	0.15	-	Ref. 5
z_0	0.033	-	Ref. 5
$\alpha_{c,0}$	0.04	-	Ref. 5
η	0.28	-	Fit.
$\eta_{el\text{-}th}$	0.43	-	Fit.
ρ_{can}	7917	$kg\ m^{-3}$	Ref. 5
ε	0.8	-	Ref. 5
ρ_{jr}	2580	$kg\ m^{-3}$	Ref. 5
$Q_{ec,max}$	36.39	kJ	Eq. 19
$\dot{Q}_{heater}$	29	W	Fit.

*The thermal conductivity of the jelly roll is anisotropic and has different values set in terms of cylindrical coordinates (r, ø, z).

each node, and the spatial average value of temperature for each time instance is coupled with the temperature term in the decomposition reactions, as shown in Figure 5.

Keeping the same number of nodes and coupling the models by using the method shown in Figure 5 reduces the number of degrees of freedom (DOF) required for solving the FEM, i.e. from 3,671,282 DOFs to 92,171 DOFs (as given by COMSOL). This results in a significant reduction of computation time, i.e. from 20,800 s to 726 s, with little influence (less than 3%) on the final results. The model was solved on an Intel Xeon 28 (56) Cores, 2.6 GHz CPU, with 256GB RAM and Fedora OS.

The 3D geometry and the position of the thermocouples can be seen in Figure 6.

The patch heaters are modeled as heat flux boundary conditions. The remaining boundary conditions are set to dissipate heat through

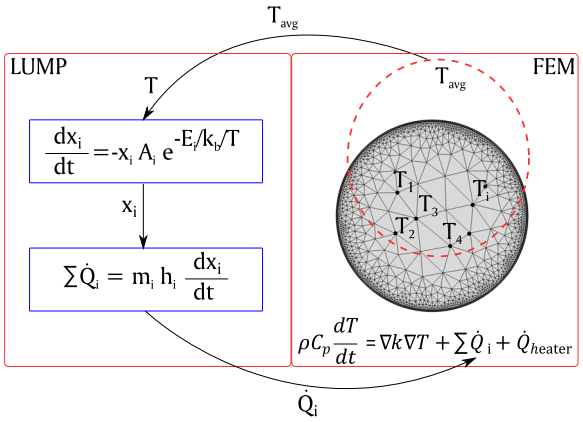

Figure 5. Coupling method between the lumped electrochemical model and the Finite Element thermal model (sketch as 2D radial section for better visual interpretation). This approach achieves faster calculation time without affecting the accuracy of the results.

convection and radiation. The jelly roll domain has a distributed volumetric heat source, which accounts for the exothermic chemical reactions and the short-circuit. Thermal conductance is added as boundary condition between the bottom cell can and the lower part of the jelly roll.[33] The equations describing the heat flux between the two domains paired in COMSOL are:

$$\begin{cases} -\boldsymbol{n}_{can} q_{can} = -h_{res}\left(T_{jr} - T_{can}\right) \\ -\boldsymbol{n}_{jr} q_{jr} = -h_{res}\left(T_{can} - T_{jr}\right) \end{cases} \quad [14]$$

The 0D model (lumped model).—The system can be reduced to a lumped model because the Biot number is very small (Bi = 0.051). By averaging the heat equation over the domain of a single battery cell, the energy balance (Eq. 7) reduces to:

$$V_{cell}\rho_{jr}Cp_{jr}\frac{dT_{avg}}{dt} = \dot{Q}_{exo} + \dot{Q}_{h,xfer} + \dot{Q}_{heater} \quad [15]$$

where $\dot{Q}_{h,xfer}$ represents the heat rate coming/leaving through convection and radiation on the boundary:

$$\dot{Q}_{h,xfer} = -A_{surf}\left[\varepsilon\sigma\left(T_{avg}^4 - T_{amb}^4\right) + h_{conv}\left(T_{avg} - T_{amb}\right)\right] \quad [16]$$

The density and the specific heat (Cp_{jr} and ρ_{jr}) of the jelly roll represent the effective properties. That is, the density and the specific heat of each component (electrolyte, electrodes, current collectors, and separators) are added on a mass basis.

The parameters for all the equations are given in Table I.

Results

Comparisons between the experiments and the model are done in terms of temperatures, considering that it is the only thermal parameter that can be easily measured experimentally. The results predicted by the lumped model are given in terms of average temperature, while the 3D temperatures are predicting the value of the temperature sensors.

Results 3D model.—For this study, the average temperature is used for triggering the reactions, as shown previously in Figure 5. The temperatures predicted by the 3D model can be seen in Figure 7.

The dashed lines correspond to the bottom and side temperatures measured on the surface of the cell. By analyzing the experimental preheat region (the region before thermal runaway), it can be seen that the bottom temperature has a higher value than the side temperatures since the heat coming from the heater is concentrated at the bottom, forming a hot area between the heaters. Right after thermal runaway, when the heater is turned off, the bottom thermocouple indicates a lower temperature. This behavior is a result of the heat that comes from

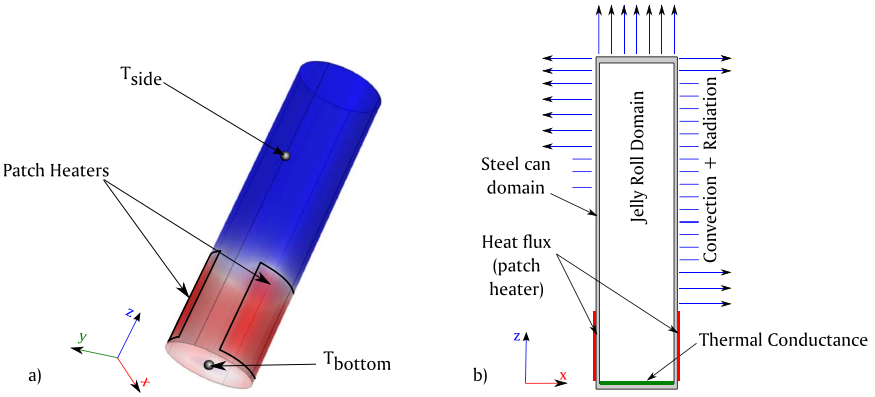

Figure 6. The 3D geometry used for modeling the single cell (a) indicating the position of each thermocouple and the patch heater and the 2D sketch of the boundary conditions and the domains (b). The 2D sketch is given only for graphical visualization of the 3D geometry.

within the jelly roll and propagates toward the bottom, dissipating heat to the ambient.

By comparing the experimental data to the model predictions, from Figure 7 it can be seen that the temperature predicted by the model follows the experimental temperature, but with some minor differences. The bottom temperature predicted by the model in the preheat region has a higher value, whereas the side temperature fits well. This difference is caused by the fact that the patch heater is modeled as a constant heat flux and there is no thermal mass in the heater. This simplification is a trade-off regarding the computation time, which would increase significantly if a FE domain would be used instead of a surface heat flux.

From Figure 7 it can also be seen that the difference between the bottom temperatures becomes significant after the peak temperature point, which reveals that a volumetric heat source is not the right approach if the bottom temperature is needed rather than the maximum peak temperature. A P2D electrochemical modeling approach[34–36] or a point/spot heat generation should be used instead of a volumetric heat source.[3] However, such an approach would complicate the model, because it requires knowing the position of the ISC with respect to the heaters. Another method would be to use a point heat source that spreads throughout the volume, but this requires finding the internal resistance of the short-circuit. Both approaches are expected to give more accurate results, but for this paper, such studies are not considered.

Results 0D model.—The 0D model for a single cell is validated against experimental data and further used for finding the efficiency factor. The 0D approach is used since it provides faster calculation times. In addition to this, it is used to prove the usability of the efficiency factor when simple ODE's are used for modeling a single cell. An efficiency factor of $\eta = 0.28$ was found when fitting the experiment; a number closer to this value is expected when analyzing the energy tally from Ref. 26. An analytical example is given at the end of this subsection.

When analyzing the temperature profile, from Figure 8 one can see the comparison between the average cell temperature predicted by the lumped model and the temperatures from the thermocouples.

Three stages can be observed in the plot:

- *the preheat stage* where the temperature increases until it reaches the melting temperature of the ISCD ($t \approx 75$ s);
- *the thermal runaway stage* where the heat released due to the short-circuit increases with a high rate causing the temperature to reach a maximum value of 700°C;
- *the cooling stage* which occurs right after the peak temperature.

The model predicts the temperature measured experimentally, which indicates that the single cell with an ISCD can be modeled using a lumped approach, which gives faster calculations. However, a distributed model is recommended if the temperature at different points on the surface is of high interest. For this paper, the analysis of the usability of the efficiency factor is of interest.

For a better description of the efficiency factor, the energy count is used for calculations. The values of the energies accumulated released by the thermal runaway are provided in Table II.

In the second column of Table II, the energy released by the anode, cathode, SEI and electrochemical reactions are given for the present model and compared with the endo- and exothermic reactions from Ref. 26. For the present paper, the venting is included in the efficiency factor, and only the exothermic reactions are added to the total tally.

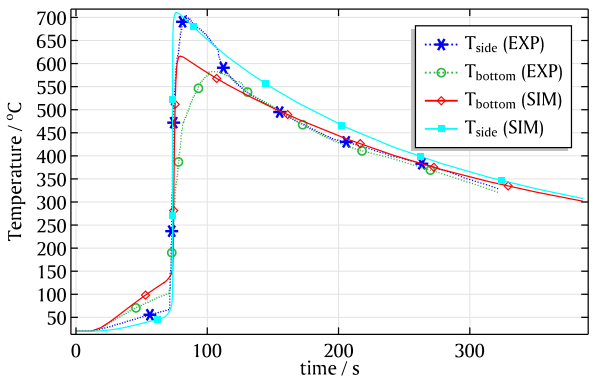

Figure 7. Comparison between the temperatures predicted by the 3D FEM and the temperatures measured experimentally in a single battery cell with ISCD, using a lumped electrochemical model and a distributed thermal model with a thermal resistance between the jelly roll and the bottom can.

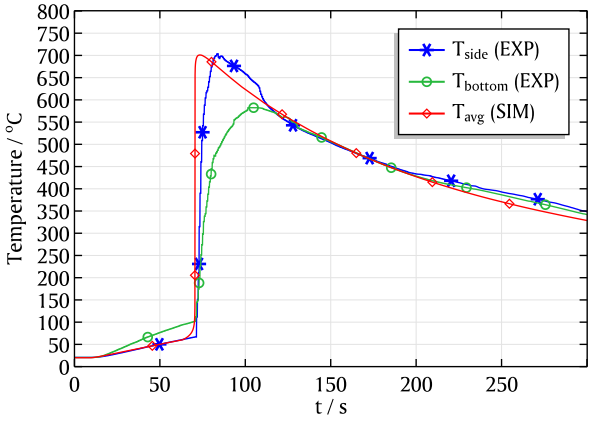

Figure 8. Comparison between the temperatures predicted by the lumped model and the temperatures measured experimentally on a single battery cell with ISCD, using a lumped electrochemical model and a lumped thermal model, and an efficiency factor of $\eta = 0.28$.

Table II. Energy tally comparison between the model with venting[26] and the model with an efficiency factor.

Source Term	Energy Contribution, kJ This Paper	Previous Work[26]
Q_a	8.2	10.4
Q_c	5.5	5.5
Q_s	0.3	0.3
Q_{ec}	10.1	15.6
Q_{vent}	0*	7.3
Q_{tot}**	24.1	24.5

*In this model venting is not included.
**The total energy is calculated as follows: $Q_{tot} = Q_a + Q_c + Q_s + Q_{ec} - Q_{vent}$.

A sample calculation for the heat sources with efficiency is given below:

$$Q_{tot} = Q_a + Q_c + Q_s + Q_{ec,max}\eta_{el-th} - Q_{vent} \quad [17]$$

where the electrochemical term represents the maximum amount of electrical energy stored in the battery cell:

$$Q_{ec,max} = V \cdot C \cdot 3600 \quad [18]$$

The thermal conversion factor ($\eta_{el\text{-}th}$) represents the conversion from electrical energy to thermal energy, and the actual electrochemical term is given as:

$$Q_{ec} = Q_{ec,max}\eta_{el-th} \quad [19]$$

By taking the values from Ref. 26 (assuming a capacity of 2.4 Ah and a voltage of 4.2 V) and calculating the electrical-thermal conversion term (from electrical energy to thermal energy), it gives $\eta_{el\text{-}th} = 0.43$ and $Q_{tot} = 24.4$ kJ. The electrical-thermal conversion term ($\eta_{el\text{-}th}$) is given in this paper only to have a separation of the composition of the efficiency term (which takes values from 0 to 1). In order to account for the venting effects, the efficiency factor (η) needs to be included, as follows:

$$Q_{tot} = Q_a + Q_c + Q_s + Q_{ec,max}\eta \quad [20]$$

The last term in Eq. 20 is equivalent to the enthalpy term from Eq. 13. By inserting the values from Ref. 26 in Eq. 20, it can be found that the calculated efficiency factor $\eta \approx 0.23$ has a value closer to the efficiency factor fitted in this paper ($\eta \approx 0.28$). There are some slight differences between this article and the previous one,[26] i.e. the cells have different thermal runaway triggering mechanism, and the energies are released/dissipated at different times. In this paper, it is assumed that all the decompositions happen around the time when the ISCD melts and triggers thermal runaway, and small differences are expected. In addition to this, the purpose of the model in Ref. 26 was to find the contribution of venting when modeling thermal runaway, and it was not validated in terms of energy count.

Conclusions and Discussion

A simplified thermal-electrochemical model was formulated using Arrhenius formulations for modeling the decomposition reactions and the short circuit in a battery cell with an ISCD embedded in the jelly roll. An efficiency factor was added to the electrochemical heat source in the energy balance equation, which accounts for the electrical energy converted into heat and also the energy that leaves due to venting. This assumption was adopted because the ISCD melts at a known temperature (T = 57°C) and triggers thermal runaway in a short time interval, meaning that all the reactions and the venting events occur at essentially the same time.

Two models were developed and validated experimentally: a 0D and a 3D model for a single cell. The models were used to match the experimental temperature of the cell only to demonstrate the ability to use the Arrhenius form with an efficiency factor by matching the maximum peak temperature and the energy tally. For the purpose of this paper, the practicality of using a single term (the efficiency factor) fitted to the experimental data was demonstrated and compared to the different models. The calculations from Eq. 16–20 showed that the energy calculated with an efficiency factor give similar results to the ones calculated with the model described in detail in Ref. 26.

It was found that the energy released by a battery cell with an ISCD is approximately the same as the energy released by a battery cell that goes into thermal runaway due to overheating. We found that 28% of the electrical energy in an 18650 (2.4 Ah) is released due to thermal runaway. Further investigations will be carried in the future for finding the scalability of the efficiency factor in batteries with different capacities.

A coupling of the electrochemical model to the thermal model was added to decrease the computation time for the 3D geometry, by using an average temperature in the Arrhenius terms, as also seen in Figure 5. Such coupling reduces the computation time from 20,800 s to 726 s without affecting the accuracy and allows the model to be used for more complex geometries.

Acknowledgments

This work was supported in part by Dr. Christopher J. Iannello, NASA Technical Fellow for Electrical Power, NASA Engineering and Safety Center, Kennedy Space Center, Florida and in part by Oticon Fonden, Denmark and Thomas B Thriges Fond, c/o Therma A/S, Denmark. The authors wish to acknowledge Steve Rickman at NASA JSC for the constant support and guidance for carrying this work and William Walker from NASA JSC for checking parts of the model.

List of Symbols

A_a	Frequency factor for anode decomposition, s^{-1}
A_c	Frequency factor for cathode decomposition, s^{-1}
A_{ec}	Frequency factor for electrochemical reactions, s^{-1}
A_{patch}	The surface corresponding to the patch heaters, m^2
A_s	Frequency factor for SEI decomposition, s^{-1}
A_{surf}	Surface exposed to convection and radiation, m^2
C	Capacity of the battery, Ah
Cp_{can}	Specific heat of the steel can, J kg^{-1} K^{-1}
Cp_{jr}	Specific heat of the jelly roll. J kg^{-1} K^{-1}
E_a	Activation energy for anode decomposition, J
E_c	Activation energy for cathode decomposition, J
E_{ec}	Activation energy for the short-circuit, J
E_s	Activation energy for SEI decomposition, J
H_{batt}	Height of the battery, m
H_{patch}	Height of the patch-heater, m
h_a	Enthalpy of anode decomposition reaction, J kg^{-1}
h_c	Enthalpy of cathode decomposition reaction, J kg^{-1}
h_{conv}	Heat transfer coefficient, W m^{-2} K^{-1}
h_{ec}	Heat released by the short-circuit, J
h_{res}	Thermal conductance jelly roll – bottom can, W m^{-2} K^{-1}
h_s	Enthalpy of SEI decomposition reaction, J kg^{-1}
ISC_{cond}	Step function with transition around the short circuit timing, -
k	Conductivity of the domain, W m^{-1} K^{-1}
k_b	Boltzmann constant, J K^{-1}
k_{can}	Thermal conductivity of the steel can, W m^{-1} K^{-1}
k_{jr}	Thermal conductivity of the jelly roll, W m^{-1} K^{-1}
m_a	Mass of anode, kg
m_c	Mass of cathode, kg
$\boldsymbol{n}$	Unit vector depicting the spatial direction, -
Q_a	Energy released due to anode decomposition, J
Q_c	Energy released due to cathode decomposition, J
$\dot{Q}_a$	Heat rate released due to anode decomposition, W m^{-3}
$\dot{Q}_c$	Heat rate released due to cathode decomposition, W m^{-3}
$\dot{Q}_{ec}$	Heat rate released due to electrochemical reactions, W m^{-3}

$\dot{Q}_{exo}$	Heat rate released due to exothermic reactions, W m^{-3}
$\dot{Q}_s$	Heat rate released due to SEI decomposition, W m^{-3}
Q_{ec}	Energy released due to electrochemical reactions, J
Q_s	Energy released due to SEI decomposition, J
Q_{vent}	Energy leaving with ejecta, J
q_{can}	Heat flux leaving/entering the steel can domain, W m^{-2}
q_{jr}	Heat flux leaving/entering the jelly roll domain, W m^{-2}
r	Radius coordinate, -
r_{cell}	Radius of the cell, m
r_{ISC}	Radius of the ISC device, m
r_{jr}	Radius of the jelly roll windings, m
T	Temperature,$^\circ$C
T_{amb}	Ambient temperature,$^\circ$C
T_{init}	Initial temperature,$^\circ$C
T_{ISC}	Melting temperature of the ISC device,$^\circ$C
t_{can}	Thickness of the steel can, m
V	Nominal voltage of the cell, V
V_{cell}	Volume of the cell, m^3
V_{ISC}	Volume of the ISC device, m^3
x_a	Fraction of Li in anode, -
x_s	Fraction of Li in the SEI, -
z	Dimensionless measure of the SEI thickness, -

Greek

α_c	Initial degree of conversion of cathode, -
η	Efficiency factor, -
$\eta_{\mathrm{el-th}}$	Electrical-thermal conversion term, -
ρ_{can}	Density of the steel can, kg m^{-3}
ρ_{jr}	Density of the jelly roll, kg m^{-3}
σ	Stefan-Boltzmann constant, W m^{-2} K^{-4}

Subscripts and Superscripts

0	Index representing initial condition
Calc.	Calculated
can	Index representing the steel can domain
EXP	Experimental
jr	Index representing the jelly roll domain
Meas.	Measured
SIM	Simulation

References

1. P. Christophe, in *Batteries*, p. 1, Nice, France (2014).
2. B. Scrosati and J. Garche, *J. Power Sources*, **195**, 2419 (2010).
3. S. Abada, G. Marlair, A. Lecocq, M. Petit, V. Sauvant-Moynot, and F. Huet, *J. Power Sources*, **306**, 178 (2016).
4. Q. Wang, P. Ping, X. Zhao, G. Chu, J. Sun, and C. Chen, *J. Power Sources*, **208**, 210 (2012).
5. T. D. Hatchard, D. D. MacNeil, A. Basu, and J. R. Dahn, *J. Electrochem. Soc.*, **148**, A755 (2001).
6. M. N. Richard and J. Dahn, *J. Electrochem. Soc.*, **146**, 2078 (1999).
7. R. Spotnitz and J. Franklin, *J. Electrochem. Soc.*, **113**, 81 (2003).
8. G. Kim, A. Pesaran, and R. Spotnitz, *J. Power Sources*, **170**, 476 (2007).
9. A. Melcher, C. Ziebert, M. Rohde, and H. J. Seifert, *Energies*, **9**, 1 (2016).
10. P. Ramadass, W. Fang, and Z. Zhang, *J. Power Sources*, **248**, 769 (2014).
11. C. J. Orendorff, E. P. Roth, and G. Nagasubramanian, *J. Power Sources*, **196**, 6554 (2011).
12. W. Cai, H. Wang, H. Maleki, J. Howard, and E. Lara-Curzio, *J. Power Sources*, **196**, 7779 (2011).
13. H. Maleki and J. N. Howard, *J. Power Sources*, **191**, 568 (2009).
14. W. Fang, P. Ramadass, and Z. Zhang, *J. Power Sources*, **248**, 1090 (2014).
15. S. Santhanagopalan, P. Ramadass, and J. (Zhengming) Zhang, *J. Power Sources*, **194**, 550 (2009).
16. W. Zhao, G. Luo, and C.-Y. Wang, *J. Electrochem. Soc.*, **162**, A1352 (2015).
17. T. Yamauchi, K. Mizushima, Y. Satoh, and S. Yamada, *J. Power Sources*, **136**, 99 (2004).
18. X. Feng, C. Weng, M. Ouyang, and J. Sun, *Appl. Energy*, **161**, 168 (2016).
19. M. Keyser, E. Darcy, D. Long, and A. Pesaran, *Pat. No. US9142829 B2* (2015).
20. M. Keyser, E. C. Darcy, and P. Ahmad, in *18th International Meeting on Lithium Batteries*, p. Poster (2016).
21. E. C. Darcy, in *18th International Meeting on Lithium Batteries*, (2016).
22. E. C. Darcy, M. Keyser, D. Long, Y. Seok, G. Heon Kim, and A. Pesaran, in *NASA Aerospace Battery Workshop*, p. 1 (2010).
23. E. Darcy, in *Sustainable Aircraft Symposium*, p. 1 (2016).
24. D. P. Finegan, E. C. Darcy, M. Keyser, B. Tjaden, O. O. Taiwo, I. Hunt, M. Scheel, M. Di Michiel, A. Rack, G. J. Offer et al., in *18th International Meeting on Lithium Batteries*, p. Poster (2016).
25. A. Pesaran and C. Yang, in *33rd Annual International Battery Seminar & Exhibit*, p. 1 (2016).
26. P. T. Coman, S. Rayman, and R. E. White, *J. Power Sources*, **307**, 56 (2016).
27. D. Carrera, *Quantum Tunneling in Chemical Reactions*, (2007).
28. W.-Y. Chang, *ISRN Appl. Math.*, **2013**, 1 (2013).
29. J. Du, Z. Liu, and Y. Wang, *Control Eng. Pract.*, **26**, 11 (2014).
30. S. Yuan, H. Wu, and C. Yin, *Energies*, **6**, 444 (2013).
31. Y. Zou, X. Hu, H. Ma, and S. E. Li, *J. Power Sources*, **273**, 793 (2015).
32. H. Fang, Y. Wang, Z. Sahinoglu, T. Wada, and S. Hara, *Control Eng. Pract.*, **25**, 45 (2014).
33. W. Walker, in *International Conference and Exhibition on Satellite*, p. 30 (2015).
34. M. Doyle, T. F. Fuller, and J. Newman, *J. Electrochem. Soc.*, **140**, 1526 (1993).
35. D. Bernardi, E. Pawlikowski, and J. Newman, *J. Electrochem. Soc.*, **132**, 5 (1985).
36. M. Doyle, J. Newman, A. S. Gozdz, C. N. Schmutz, and J.-M. Tarascon, *J. Electrochem. Soc.*, **143**, 1890 (1996).
37. H. Maleki, S. Al Hallaj, J. R. Selman, R. B. Dinwiddie, and H. Wang, *J. Electrochem. Soc.*, **146**, 947 (1999).
38. A. W. Golubkov, D. Fuchs, J. Wagner, H. Wiltsche, C. Stangl, G. Fauler, G. Voitic, A. Thaler, and V. Hacker, *RSC Adv.*, **4**, 3633 (2014).
39. M. Keyser, G. Kim, and A. Pesaran, *Numerical and Experimental Investigation of Internal Short Circuits in a Li-ion Cell*, (2011).